ACS Energy LETTERS

Cite This: ACS Energy Lett. 2020, 5, 23−30

http://pubs.acs.org/journal/aelccp

LETTER

Rational Design of 2D Manganese Phosphate Hydrate Nanosheets as Pseudocapacitive Electrodes

Kumar Raju,*[,†] Hyungkyu Han,[‡] Dhinesh Babu Velusamy,[§] Qiu Jiang,[§] Huachao Yang,[∥] Funeka P. Nkosi,[⊥] Nithyadharseni Palaniyandy,[†] Katlego Makgopa,[#] Zheng Bo,[∥] and Kenneth I. Ozoemena*[,▽]

[†]Energy Centre, Council for Scientific and Industrial Research (CSIR), Pretoria 0001, South Africa

[‡]Energy and Environment Directorate, Pacific Northwest National Laboratory, Richland, Washington 99352, United States

[§]Division of Physical Sciences and Engineering, King Abdullah University of Science and Technology (KAUST), Thuwal 23955-6900, Kingdom of Saudi Arabia

[∥]State Key Laboratory of Clean Energy Utilization, Zhejiang University, Hangzhou, Zhejiang 310027, China

[⊥]Department of Chemistry-Ångström Laboratory, Uppsala University, SE-75121 Uppsala, Sweden

[#]Department of Chemistry, Tshwane University of Technology, Pretoria 0001, South Africa

[▽]Molecular Sciences Institute, School of Chemistry, University of the Witwatersrand, Private Bag 3, Johannesburg 2050, South Africa

Supporting Information

ABSTRACT: **A new class of 2D nanosheets of nitrogen-integrated phosphate-rich ammonium manganese phosphate hydrate, ($NH_4MnPO_4 \cdot H_2O$) (AMP), has been developed as pseudocapacitive electrode materials. The optimized electrodes exhibited device capacitances of 48.4 and 65.4 F/g for symmetric and asymmetric configurations, respectively. The devices showed excellent energy and power (e.g., 29.4 Wh/kg and 133 kW/kg for asymmetric cells) with extraordinary capacitance retention (e.g., >93%, 100 000 cycles at 5 A/g for asymmetric cells) that surpass those of most of the reported values. The huge pseudocapacitance of AMP is attributed to several factors, including the electroactive sites containing NH_4^+ ions, the conductive inorganic layers, intercalated water interactions of $Mn^{2+}\cdots H_2O$, redox-active phosphate ions, and the 2D nanosheets. AMP-based all-solid-state flexible asymmetric devices exhibited >95% capacitance retention upon 1000 repetitive charge−discharge cycles. This study opens doors to elegant strategies of unlocking the rich physicoelectrochemical properties of 2D AMP for next-generation pseudocapacitors.**

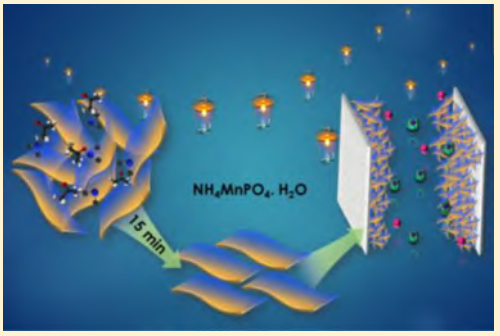

Depletion of fossil fuels and ever-increasing demands of energy are major obstacles to modern day society. It is thought that these challenges could be altered by innovative and contemporary ideas for zero pollution or a low-carbon footprint.[1−4] Although energy storage and conversion devices are being envisioned as potential players in energy technology and to afford cleaner energy, new materials with combined high energy and high power are urgently needed.[5−11] Among the electrochemical energy storage devices, supercapacitors are being identified as cleaner energy storage devices that will drive next-generation portable, flexible, and wearable electronics and, importantly, will also play a pivotal role in the large-scale availability of electrical vehicles, smart power grids, and intermittent energy sources.[12−17] However, achieving a high-performance active electrode material that can surpass the performance of conventional carbon-related materials has particularly been quite challenging. In fact, some of the key challenges of all-carbon-based supercapacitors include poor energy density as well as the need to functionalize them with heteroatoms such as nitrogen, phosphorus, and sulfur to enhance their conductivity and stability and improve the electrosorption of ions in electrical double-layer capacitors (EDLCs) (i.e., non-Faradaic process, only charge accumulations at the electrode−solution interface, no electron transport). Therefore, developing an entirely new

Received: October 20, 2019
Accepted: November 19, 2019
Published: November 19, 2019

DOI: 10.1021/acsenergylett.9b02299
ACS Energy Lett. 2020, 5, 23−30

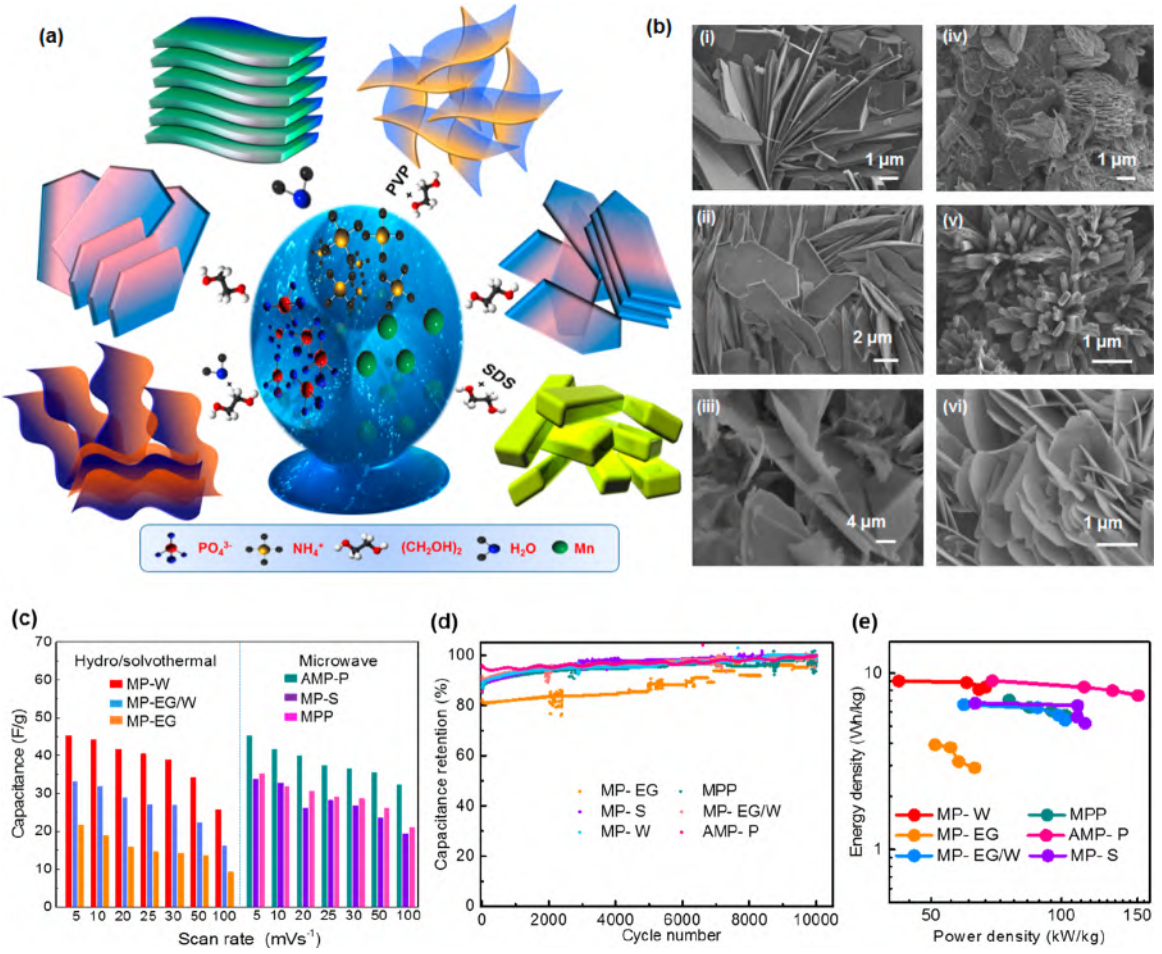

Figure 1. Schematic representation for the formation of different polymorphs of manganese phosphate by different preparation routes and electrochemical performances obtained in symmetric pseudocapacitor devices for all six different morphologies synthesized. (a) Synthesis route possessed for all six different morphologies by microwave and hydro/solvothermal processes using water and EG as solvents and polyvinylpyrrolidone (PVP) and sodium dodecyl sulfate (SDS) as surfactants. Various morphologies like (b) layered microsheets (i), hexagon-like microsheets (ii), microdendrites (iii), pentagon-like microsheets (iv), microbelts (v), and thin microsheets (vi) were obtained by reacting the mixture of EMD (MnO_2) with ammonium dihydrogen phosphate in the presence of EG as the solvent for microwave irradiation and a mixture of water and EG for hydro/solvothermal synthesis. (c) Capacitance calculated from CV curves of the symmetric device at different scan rates ranging from 5 to 100 mV/s for all morphologies synthesized. (d) Cycling stability test employed for all morphologies at a current density of 0.5 A/g for about 10 000 consecutive cycles. (e) Ragone plot of the energy and power density for MPP, MP-EG, MP-EG/W, MP-S, MP-W, and AMP-P microstructures.

type of active electrode material with inherent properties to maximize both surface area and electrical conductivity is crucial for robust energy storage devices. Recently, two-dimensional (2D) nanomaterials like the chalcogenides, metal carbides/nitrides (MXene),[18,19] metal phosphides,[20] metal phosphates,[12,21] and MOF[22] have shown promise for the development of high-energy-density supercapacitors due to their outstanding electrochemical properties.

A class of materials that can hold the heteroatoms in their structure and allow for fast ion propagations are nitrogen-integrated phosphate-rich materials (PRMs) such as $NH_4NiCoPO_4{\cdot}H_2O$,[23] layered $NH_4CoNiPO_4{\cdot}H_2O$,[24] and 2D $VOPO_4$ nanosheets.[12] Although the PRMs have been reported as high-performance pseudocapacitor materials, the dynamic electron- and ion-transfer processes involving all active sites of the electrode materials remain a challenge. PRMs are characterized by limited electronic conductivity and non-compatible conduction pathways, thus their inherent high electrode resistance and low power densities. Therefore, unique design strategies that will allow the development of a novel electrode architecture with excellent ability to generate exceptional surface redox storage at high rate capabilities cannot be overemphasized.

Heteroatom-integrated PRMs possess unique structural properties that are attractive for energy storage applications: NH_4^+ ions attached between the conductive inorganic layers via hydrogen bonding enable rapid electron transport to the electroactive sites; edge-shared highly distorted octahedral MnO_6 and corner-shared cross-linked tetrahedral PO_4^{3-} are highly redox-active; intercalated water interactions (i.e., $NH_4^+\cdots H_2O$ and $Mn^{2+}\cdots H_2O$) assist in rapid ion transport; two-dimensional nanosheets boost both electronic and ionic transports; minimized restacking of 2D nanosheets by exfoliation helps to maintain the structural integrity of the electrodes.[25] According to the literature, ammonium manganese phosphates (AMPs) have been used only for electromagnetic applications,[26,27] and very recently, they have been reported as precursor materials to form olivine-type electrode materials for lithium-ion batteries.[28]

DOI: 10.1021/acsenergylett.9b02299
ACS Energy Lett. 2020, 5, 23−30

In this work, a liquid exfoliation strategy has been developed to tune the morphology of AMPs to obtain well-resolved 2D nanosheets with high aspect ratio and high surface area. A facile strategy is introduced to design the various polymorphs of 2D manganese phosphates by microwave irradiation and solvo/hydrothermal treatment of electrolytic manganese oxide (EMD), δ-MnO_2, and ammonium dihydrogen phosphate in ethylene glycol (EG), H_2O (W), and EG/W mixed solvents with the use of different surfactants. The synthesis conditions of AMP-P and MP are considerably milder than the harsh chemical treatments used to make graphene and MXene. Herein, it is demonstrated how the nanosheets of AMP architecture, along with confinement of electrons and ions, enable exceptional surface redox kinetics.

The synthetic strategies adopted to tune the morphology of the phosphate-rich layered AMP-P hydrate, polymorphs of manganese orthophosphates (δ-, γ-$Mn_3(PO_4)_2$), and $Mn_3(PO_4)_2{\cdot}3H_2O$ (denoted herein as MP-W, MP-EG and MP-EG/W)), and manganese(II) pyrophosphate ($Mn_2P_2O_7$ (MPP)) via microwave and solvo/hydrothermal methods, with and without surfactants, in two different solvent media of EG and W are schematically illustrated in Figure 1a. The different polymorphs of $Mn_3(PO_4)_2$ achieved via the solvo/hydrothermal route exhibited well-exposed thicker layers compared to the layered manganese phosphates obtained using the microwave irradiation route alone. The 2D structure, obtained by microwave synthetic route gave thinner layers of AMP-P (i.e., obtained in EG but with PVP surfactant) with proper pore structures that can speed up the ion propagations along with the surface interactions at the interface. The formation mechanism of layered manganese phosphates involves the insertion of large metal ions like Mn^{2+} into the NH_4^+ and PO_4^{3-} structural blocks that results in the formation of a 2D structure. The diffusion of ions is enhanced with a rise in temperature, thus enhancing the nucleation processes.[29] The synthesized layered transition metal phosphates and their hydrate forms (i.e., $Mn_2P_2O_7$, δ-$Mn_3(PO_4)_2$, and γ-$Mn_3(PO_4)_2$ and $Mn_3(PO_4)_2{\cdot}3H_2O$ and $NH_4MnPO_4{\cdot}H_2O$) were confirmed by powder XRD analysis (see Supporting Information, Figure S1a–c for detailed structural information). In summary, the XRD patterns exhibited a cubic structure with $P2_1/c$, $P2_1/n$, and $P2_1/a$ space groups of MP-W, MP-EG and MP-EG/W, and $NH_4MnPO_4{\cdot}H_2O$ (space group: $Pmn2_1$, lattice parameter a = 5.71 Å, b = 8.83 Å, and c = 4.87 Å, JCPDS # 50-0554, card # 9012524) and $Mn_2P_2O_7$ (space group: $C2/m$, JCPDS # 29-0891).

Various 2D nanostructured morphologies from layered microsheets to belts and flowers were confirmed from SEM and TEM analyses. The images (shown in Figure 1b(i–vi) as well as in the Supporting Information Figures S2 and S13) demonstrate how the synthetic strategy led to well-resolved diverse architectures/morphologies with average dimensions of 1 μm in length and 45–250 nm in width. Figure S2a–c exposes the thick layered $Mn_2P_2O_7$ (MPP) with an average micrometric length and width (Figure S2b) with the corresponding lattice fringe (d = 0.55 nm). The d-spacings of the lattice fringes are found to be 0.570 and 0.567 nm, matching with (121) planes of MP-W (Figure S2d–f) and MP-S (Figure S2g–i) and showing microplates with nanometric length (Figure S2). In comparison, the nanosheets of AMP-P with ~45 nm width greatly exposed the (010) plane with a d-spacing of 0.57 nm compared to the (121) plane (d = 0.32 nm) (Figure S2j–l) and different dimensions of nanometric width of *ca.* 250 nm thick microsheets (MP-W), 218 nm (MP-EG), 140 nm (MP-EG/W), and 97.6 nm (MP-S) (Figure S2). The thickness of the AMP-P thin layers decreased further when the liquid exfoliation was performed at different time intervals (Figure S3). The elemental mapping and composition analyses confirm the formation of well-defined AMP-P (Figure S3). The height profile measurement by AFM analysis is also confirmed by the decreasing layer thickness at different exfoliation time intervals and the height profiles of nanosheets found to be ~45, 30, and 27 nm, respectively, at different time intervals such as 5, 10, and 15 min (Figure S4). It is very interesting to observe that microwave irradiation and the surfactants used in the synthesis conferred adequate dimensionality on the materials that permits efficient and rapid redox processes.

Figures 1c–e and S5 compare the electrochemical performance of the symmetric devices of the six different morphologies in a 3 M KOH aqueous solution. Well-resolved rectangular cyclic voltammetric (CV) curves with bulk AMP-P thin sheets giving a higher electrochemical surface activity (i.e., high current response) are attributed to confined ion transfer with a shorter diffusion path and high surface area (Figures S5a and S12 and Table S1). However, well-defined redox couple arose from the redox-active $Mn^{3+}/^{4+}$ with a small cathodic and anodic peak potential separation (ΔE_p) of 96 mV for AMP-P (Figure S6b) when compared to other microstructures investigated, as depicted in Figure S6a and S14, indicating a satisfactory redox process. Besides, the structure–property relationship and morphology tunings of δ-$Mn_3(PO_4)_2$ (MP-W) and AMP-P are effectively pronounced as they show higher electrochemical surface activity than the other counterparts (such as MPP, MP-S, MP-EG/W, and MP-EG) with a high specific capacitance of 423 F/g (AMP-P) at a scan rate of 5 mV/s (mass loading of 2.25 mg/cm^2), a value that is much higher than literature findings such as the MXene hydrogel (350 F/g).[18] Figure 1c further proves that the symmetric devices of MP-W and AMP-P achieved higher capacitances of 45 and 45.3 F/g at a scan rate of 5 mV/s and retained their initial capacitances of about 57 and 71% at a higher scan rate of 100 mV/s, respectively. The obtained specific capacitance value of MP-W is higher than that reported for $Mn_3(PO_4)_2{\cdot}3H_2O$ pseudocapacitors.[30] The obtained Nyquist plots for all microstructures (both in three-electrode and full cell symmetric cell configurations) revealed a low ion transport resistance with an almost linear curve at a low frequency domain (a typical supercapacitor behavior) with higher knee frequency (low response time). Figures S8e and S5b show the Nyquist plots obtained for all microstructures in the half-cell and symmetric device in a 3 M KOH aqueous solution.

Table S2 summarizes the EIS data of series resistance (R_s), charge-transfer resistance (R_{ct}), and response time (τ_0). The symmetric device of AMP-P showed very low R_s = 0.23 Ω with a response time of 18 ms when compared to the other microstructures analyzed. Besides, a similar trend is observed in the half-cell configuration as well; the AMP-P showed that R_s = 0.53 Ω with a response time of 18 ms was lower than the values reported in liquid electrolyte used in supercapacitors and onion-like carbon (26 ms).[31] The low resistance value and high power capability of AMP-P clearly demonstrate the excellent ion propagation process of this material. Figure 1d compares the cycling stability of all six microstructures in a symmetric configuration at 1 A/g, achieving ca. 97% capacitance retention (as also seen with the half-cell

DOI: 10.1021/acsenergylett.9b02299
ACS Energy Lett. 2020, 5, 23–30

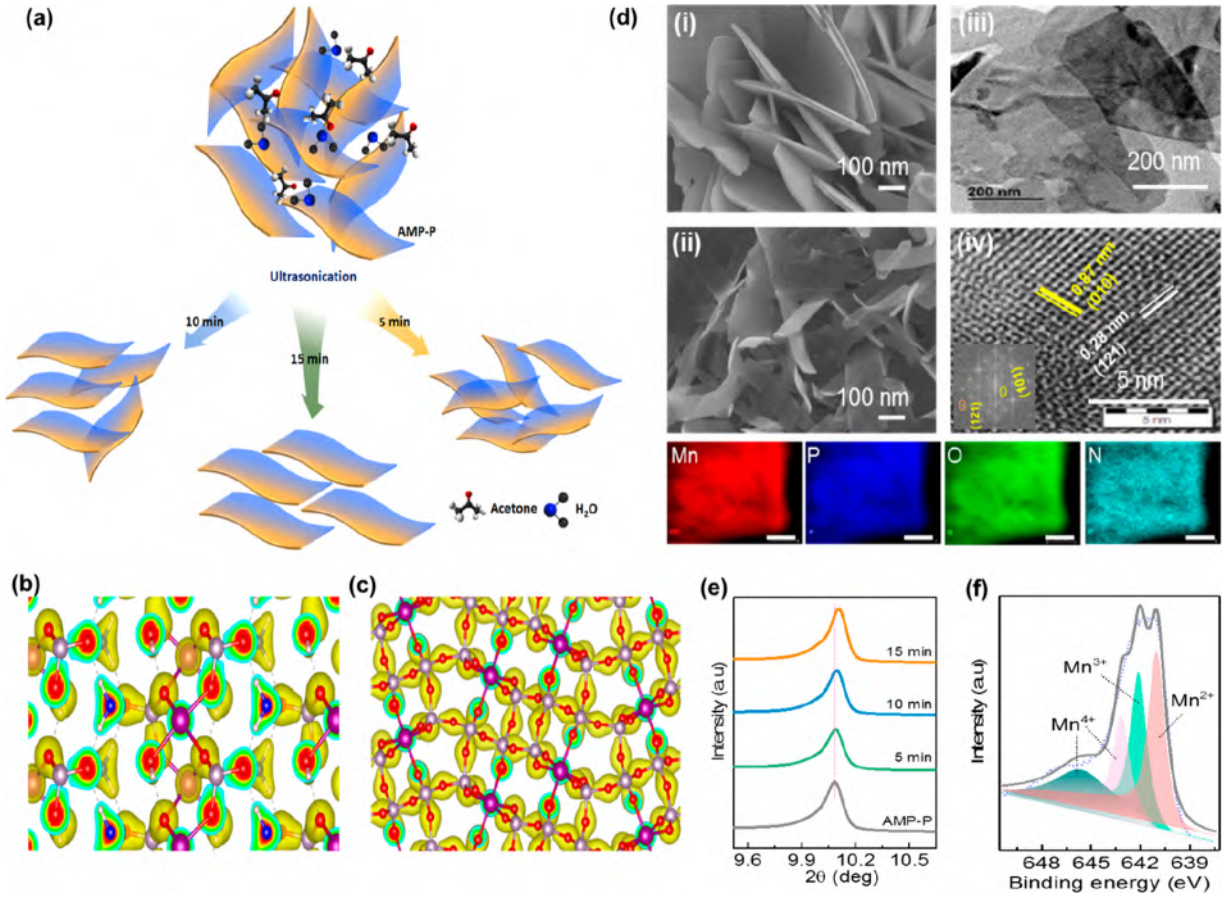

Figure 2. Physical and electrochemical performance of exfoliated ammonium manganese phosphate nanosheets (AMP-P) performed by ultrasonication for 5, 10, and 15 min. (a) Schematic representation of ultrasonication for three different time intervals of 5, 10, and 15 min. Electron density of (b) AMP-P and (c) MP-W (isovalue is set as 0.1 e × Å^{-3}) observed based on the DFT calculation. (d) Morphological evolution of AMP-P-15: scanning electron microscopy (SEM) images of AMP-P (i), exfoliated nanosheets of AMP-P by ultrasonication in 15 min (ii), HR-TEM image of highly delaminated AMP-P nanosheets with 15 min sonication (iii), and lattice fringe and SAED pattern (inset) of AMP-P-15 min with a calculated interplanar distance value of 0.87 nm corresponding to the (010) plane and the lattice fringe of 0.21 nm corresponding to the (121) plane (iv). Colored images named Mn, P, O, and N represent the elemental mapping of highly distributed elements of manganese, phosphorus, oxygen, and nitrogen in the AMP-P-15 min nanosheets; scale bar: 80 nm. (e) Powder X-ray diffraction (PXRD) pattern of exfoliated AMP-P nanosheets in different time intervals of 5, 10, and 15 min. (f) High-resolution X-ray photoelectron spectroscopy (XPS) profile of Mn $2p_{3/2}$ of the 15 min exfoliated AMP-P sample.

configuration, Figure S8a) with the AMP-P delivering higher capacitance. The MP-EG microstructure delivers low capacitance retention. As shown in Figure 1e, the Ragone plot describes the power and energy densities at the different current densities, and it was found that the AMP-P achieved higher energy and power values (9.7 wh/kg and 150 kW/kg) compared to those of other microstructures.

Figure S9a−d compares how the AMP-P and MP-W perform better than other polymorphs. $NH_4MnPO_4{\cdot}H_2O$, a polymorph of the niahite structure (Figure S9a), formed through the sharing of highly distorted MnO_6 octahedral corners cross-linked with oxygen atoms of phosphate tetrahedra and NH_4^+ ions inserted between the inorganic layers via hydrogen bonding. The lower surface energy of the (010) plane in AMP leads to a layer growth mechanism along the axis of its crystalline phase. The layered structure formed due to the superexchange interactions of the Mn−O−P−O−Mn- and Mn−O−Mn-type bonding leading to the formation of tetrahedra−octahedra−tetrahedra (TOT) layers along the *c*-axis with definite diameter channels favors the formation of a sheet-like morphology, anisotropically, without the addition of any surfactants.[32−34] However, surfactants like PVP and SDS assist in the formation of definite structures like thinner sheets and belts. It is worth mentioning here that the intermolecular dehydration of NH_4MnPO_4 occurred very quickly via microwave irradiation, resulting in the formation of a layered $Mn_2P_2O_7$ structure, which is well-known to be very difficult to obtain via low-temperature synthesis; in fact, most of the reported $Mn_2P_2O_7$ species are nonlayered.[26] Interestingly, an important polymorph of δ-$Mn_3(PO_4)_2$ (Figure S9c) was achieved by a facile hydrothermal route; however, the bonding structure differs from that of other polymorphs as it shares MnO_5 pentahedral corners and edges with phosphate tetrahedra (with no MnO_6 octahedral coordinate sites), thus leading to the formation of a low-density porous material, which is suitable for efficient energy storage.

Figure S9b,d shows the unit cells of AMP-P and MP-W used to carry out the DFT calculations. The preferential paths for electron distribution are pictorially shown in Figure 2b,c. The structure suggests that the electrons are mainly distributed on oxygen and nitrogen for the AMP-P and on oxygen only for the MP-W. The densities of states of the stimulated structures of AMP-P and MP-W are presented in Figure S9e,f. It is clear that the valence states are strongly correlated with the mixing

DOI: 10.1021/acsenergylett.9b02299
ACS Energy Lett. 2020, 5, 23−30

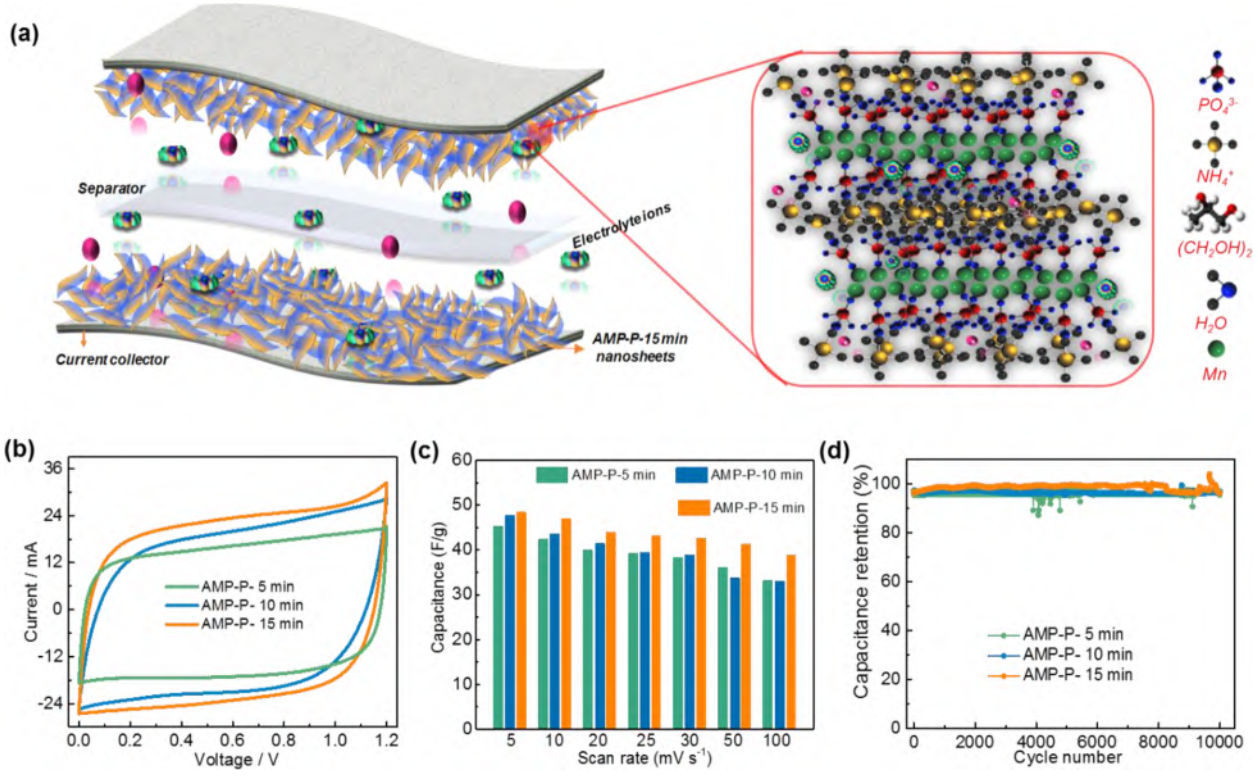

Figure 3. (a) Schematic illustration of the working principle of a symmetric supercapacitor device constructed with exfoliated AMP-P nanosheets in an aqueous electrolyte of 3 M KOH; OH^- ions are inserted and deinserted onto the Mn site (Mn(OH), e.g., $NH_4Mn(OH)PO_4$), as shown in the magnified view. (b) CV curves of AMP-P exfoliated over different time intervals exposed almost rectangular shaped redox behavior; 15 min exfoliated nanosheets achieved the highest current response. (c) Device capacitance calculated from CV curves at different scan rates ranging from 5 to 100 mV/s. (d) Cycling stability test employed for AMP-P-5 min, AMP-P-10 min, and AMP-P-15 min at a current density of 0.5 A/g for about 10 000 consecutive cycles.

of the 3d orbitals of Mn and the P orbitals of oxygen, while the conduction band minimum formed primarily of the 3d orbitals of Mn, with a calculated bandgap of 1.73 eV for AMP-P and 2.27 eV for MP-W. Although the MP-W shows a low-density layered structure, a large bandgap is largely responsible for its low conductivity, hence its poor electrochemical performance compared to that of the AMP-P.

The AMP-P microsheets were further exfoliated in the acetone−water mixture to expose the ultrathin nanosheets with (010) surface facets. Typically, ultrasonication aids the delamination of AMP-P interlayers, which are swallowed by acetone−water mixture insertions into the interlayer spaces via hydrogen bonding. Figure 2a systematically demonstrates the exfoliation processes of the AMP-P at different time intervals (5, 10, and 15 min) to enhance the delamination of the nanosheets. An ultrasonication of 15 min exposure time leads to the formation of transparent ultrathin nanosheets ∼200 nm in width (∼300 nm in length) and highly desirable surface facets of (010), as depicted of SEM and HRTEM images in Figure 2d(i−iv). Figures 2d(ii,iii) and 3 S3 depict the excellently exfoliated nanosheets of AMP-P-15 min with a lateral size of ∼300 nm (Figure 2d(iii)) from the tightly stacked microsheets. The SAED (inset Figure 2d(iv)) pattern of AMP-P-15 min reveals a calculated *d*-spacing value of 0.87 nm, corresponding to the (010) plane, confirming the preferential crystal growth orientation. Elemental mapping from energy-dispersive X-ray analysis (EDX) clearly identifies manganese, phosphate, oxygen, and nitrogen in AMP-P (displayed in Figure 2d as Mn, P, O, and N, respectively). Figures 2e and S1c show the PXRD pattern of AMP-P at different time intervals, further confirming the preferential orientation of the (010) plane. The peak intensity increases with an increase in the exfoliation time; indeed, the sonication time triggers structural rearrangements along the unique axis for the formation process of the ultrathin nanosheets, as shown in the projection of the $Pmn2_1$ space group of the AMP layer structure with the *c*-axis (Figure S9). High-resolution XPS analysis proves the chemical states of AMP-P-15 min in comparison with MPP (Figures 2f and S10). The binding energy of the Mn $2p_{3/2}$ orbitals clearly demonstrates the initiation of mixed valence states of manganese, and it should be noted that the existence of a higher Mn^{4+} concentration in AMP-P-15 min means that this material is capable of significantly suppressing the Jahn−Teller distortion, which is critical for long-term cycling stability.

Figure 3a illustrates the working principle of a symmetric supercapacitor device constructed using the exfoliated nanosheets of AMP-P coated on a nickel foam current collector in a 3 M KOH solution. The magnified view depicts the network topology of insertion and deinsertion of electrolyte ions into the Mn active site, demonstrating the 2D-confined electrons and ion propagation. Figures 3b−d and S5c−e summarize the electrochemical performance of all exfoliated nanosheets. Figure 3b compares the CVs of the exfoliated AMP-P nanosheets and shows the highest current response for the AMP-P-15 min electrode.

The shape of the CV curves did not show noticeable redox peaks as observed in the three-electrode system (Figures S2

DOI: 10.1021/acsenergylett.9b02299
ACS Energy Lett. 2020, 5, 23−30

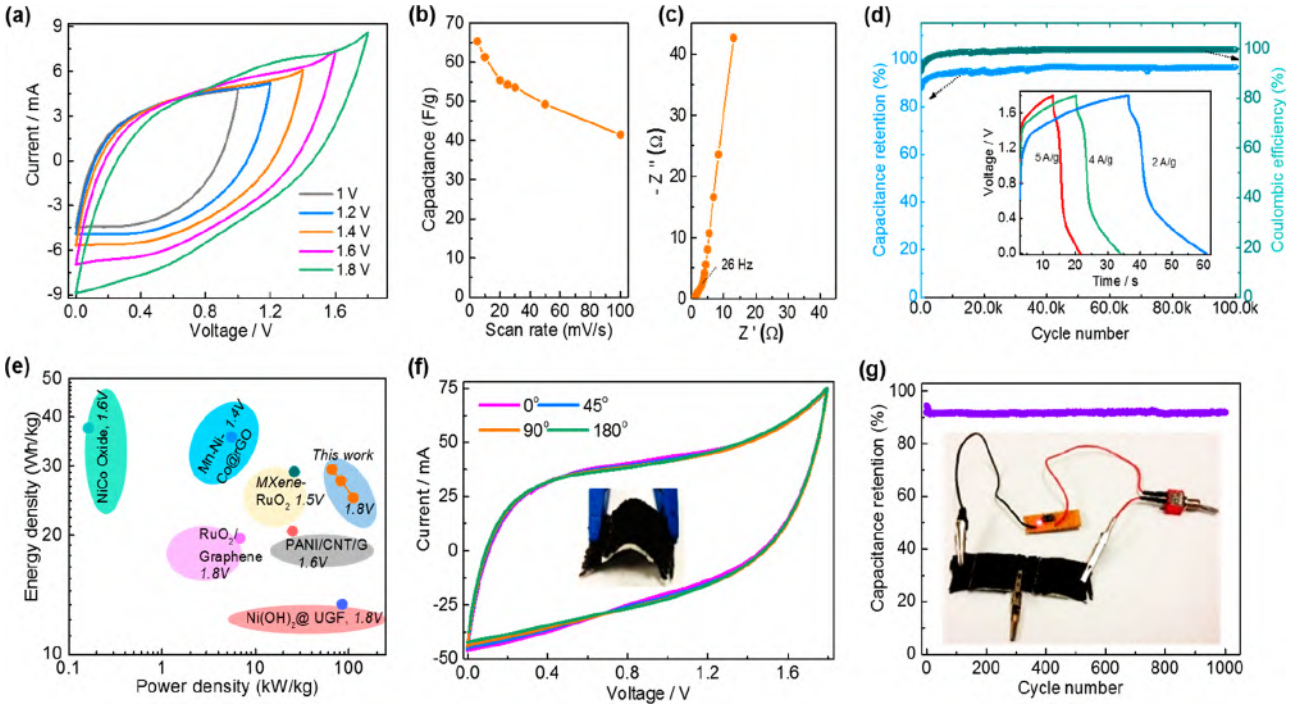

Figure 4. Electrochemical performances of the asymmetric supercapacitor device constructed with AMP-P-15 min against Nurit supra carbon in 3 M KOH aqueous solution and all-solid-state flexible devices fabricated with PVA/KOH gel polymer electrolyte. (a) CV profile of the asymmetric device examined in different voltage windows ranging from 1 to 1.8 V. (b) Device capacitance calculated from CV profiles at different scan rates ranging from 5 to 100 mV/s. (c) Nyquist plot of the asymmetric device examined in the frequency range from 1 MHz to 10 mHz at room temperature. (d) Cycle stability test employed at a current density of 5 A/g for about 100k consecutive cycles; the inset shows the charge−discharge plots obtained at current densities of 2, 4, and 5 A/g. (e) Ragone plot of the asymmetric device compared with energy and power densities of some of the reported literature results. (f) CV plots of the asymmetric device at different bending angles such as 0, 45, 90, and 180° at a scan rate of 25 mV/s; the inset shows the photograph of the asymmetric device fabricated in a carbon cloth current collector at different bending angles. (g) Durability of the all-solid-state device with almost 95% capacitance retention at a current density of 1 A/g; the inset shows a digital photograph of the two asymmetric devices connected in series and lighting up a 1.67 V LED.

and S6a) nor the ideal rectangular shapes of the EDLC but contributions from both the EDLC and pseudocapacitor. Figure S5c shows typical galvanostatic charge−discharge profiles of the symmetric cell obtained at current densities of 2 and 3 A/g. The slightly lower Coulombic efficiency (<100%) at the lower rate (2 A/g) compared to 100% at the high rate (3 A/g) may be related to series resistance. In general, the Coulombic efficiency improves at a high rate and/or after a long cycling process (see, for example, Figure S7). Figure S5d compares the Nyquist plots obtained for the electrodes. The differences in pseudocapacitive behavior are due to the level of interfacial impedance, where the AMP-P-15 min is much better than the AMP-P-5 min by showing the least resistance (as clearly corroborated in Table S2). The symmetric device of AMP-P-15 min delivered an exemplary gravimetric capacitance of 48.4 F/g at a scan rate of 5 mV/s with an excellent rate performance of 38.8 F/g (80%) at a scan rate of 100 mV/s (Figure 3c). The symmetric device exhibited excellent cycle stability with only ∼3% capacitance loss upon 10 000 consecutive galvanostatic charge−discharge cycles (Figure 3d).

The total stored charge in a battery-like material can be divided into (i) a capacitive-controlled process (i.e., Faradaic fast charge-transfer process on the surface and non-Faradaic contribution from the double-layer adsorption) and (ii) a diffusion-controlled Faradaic process due to an ion intercalation process (battery-like phenomenon). To distinguish and quantify the contribution from the capacitive charge storage mechanism from the total current response, the measured current response, i, from the CV at different scan rates, υ, obeys the power law relationship[35,36]

$$i = a\upsilon^{b} \tag{1}$$

where a and b are adjustable parameters. The measured slope b value indicates the predominant contributions; if b = 0.5, it is mainly by the diffusion-controlled process, and if b = 1, it is dominated by capacitive process. Figure S11c−f clearly indicates that both the half-cell and symmetric device show a b value more than 0.5, inferring that the current response is mainly contributed by the capacitive process. The capacitive contribution to the overall current response can be separated by

$$i(V) = k_1\upsilon + k_2\upsilon^{1/2} \tag{2}$$

where υ is the scan rate (mV/s) and $k_1\upsilon$ and $k_2\upsilon^{1/2}$ are the obtained currents from the capacitive contribution and diffusion-controlled Faradaic contribution, respectively.

$$\frac{i(V)}{\upsilon^{1/2}} = k_1\upsilon^{1/2} + k_2 \tag{3}$$

A linear plot can be obtained by modifying eqs 2 and 3, and k_1 and k_2 can be derived from $i(V)/\upsilon^{1/2}$ versus $\upsilon^{1/2}$ with different scan rates. Figure S11a,b clearly indicates the predominant contributions of the capacitive process, found to be ∼60% for the half-cell and 75% for the symmetric device at a scan rate of 20 mV/s.

DOI: 10.1021/acsenergylett.9b02299
ACS Energy Lett. 2020, 5, 23−30

The EIS of AMP-P-15 min confirms excellent power capability with low R_s = 0.19 Ω when compared to 10 and 5 min exfoliated counterparts (R_s = 0.22 and 0.23 Ω) with a response time of ∼12 ms (Figure S5d, Table S2), clearly confirming the high electrical conductivity. As shown in the Ragone plot (Figure S5e), the AMP-P-15 min device showed a high energy of 9.7 Wh/kg at a scan rate of 5 mV/s, and even at a high scan rate of 100 mV/s, the device gave a high energy density of 7.8 Wh/kg.

To extend the operational voltage and further increase the energy density, an asymmetric device configuration was fabricated with activated carbon (Nurit supra) as a negative electrode in 3 M KOH solution; the operating potential window explored from the three-electrode measurements is from −1.0 to 0.0 V at the anode and 0.0 to +0.5 V at the cathode (Figure S15a). Importantly, the asymmetric device showed quasi-rectangular CV curves with an expanded voltage window of 1.8 V (Figure 4a) in contrast to the symmetric device with an operating voltage window of 1.2 V.

The battery-like galvanostatic charge−discharge profiles obtained for the asymmetric device are due to the predominant surface redox kinetics, i.e., pseudocapacitive behavior (Figure 4c, inset) with a capacitance of 65.4 F/g at a scan rate of 5 mV/s, and the device maintains a capacitance of 42 F/g even at a higher scan rate of 100 mV/s (Figure 4b). This high rate capability of AMP-P-15 min is evident with its low response time of 38 ms with very low resistance (R_s = 0.79 Ω) (Figure 4c) compared to literature values, such as MXene-RuO_2 (740 ms).[35] As depicted in Figure 4c, the asymmetric device showed an extraordinary cycle stability with capacitance retention of ∼93% upon 100k continuous charge−discharge cycles with 100% Coulombic efficiency. The Ragone plot (Figure 4e) of the asymmetric device exhibits higher energy (29.4 Wh/kg at 5 mV/s) and power (133 kW/kg) densities when compared with those of other asymmetric capacitors, such as MXene-RuO_2 (29 Wh/kg and 26 kW/kg),[35] GO/MnOx (29.7 Wh/kg and 20.8 kW/kg),[37] OLC/Mn_3O_4 (19 Wh/kg and 45 kW/kg),[38] 3D-C/Co-NiO (19.2 Wh/kg and 13 kW/kg),[39] and so many others (see Table S3).

The post-mortem analysis (Figure S17) clearly confirms the structural stability of the AMP-P-15 min. After a prolonged cycling test, the EIS showed that the material gains only little resistance. Interestingly, there was only a slight increase in charge-transfer resistance, from 30 to 40 Ω (i.e., 0.0001 Ω per cycle), but with the inclined (90° line) becoming much better after 100k cycles (i.e., enhanced pseudocapacitor behavior). The FESEM images confirm that the AMP-P-15 min retains almost its sheet-like morphology with some aggregated particles on it, and the XRD results also infer that the sample retains its lattice structure with some impurities along with the carbon cloth substrate (Figure S17). The volumetric energy densities of the AMP-P-15 min electrode with higher mass loading against the scan rate were estimated to be ∼0.53 and 0.39 Wh/cm^3 for 2.5 and 5 mg/cm^2 mass-loaded electrodes, respectively (Figure S18). The volumetric energy density achieved with high mass loading is better than that of the MnO_2-based asymmetric device.

All-solid-state flexible and wearable asymmetric devices were constructed with AMP-P-15 min and activated carbon on carbon fabric in a PVA-KOH polymer gel electrolyte. As a proof-of-concept, the prototype all-solid-state flexible asymmetric device showed its flexibility by measuring the CVs with various bending angles and obtained almost the same CV characteristics, even when the device was bent to 180°, as shown in the digital photograph of different angles (Figures 4f and S16). To ensure the real application of our device, the two flexible asymmetric devices were connected in series to deliver 3 V (Figure S15b) and were able to light up a 1.67 V LED, as shown in the inset of Figure 4g. Importantly, the asymmetric flexible device retained almost 95% of its initial capacitance upon 1000 consecutive galvanostatic charge−discharge cycles (Figure 4g).

In summary, supercapacitive properties of various novel polymorphs of 2D manganese phosphates have been studied. Exfoliated nanosheets of ammonium manganese phosphate hydrate outperform, with a voltage window of 1.2 V for symmetric and 1.8 V for asymmetric devices, and showed capacitance retentions of 80% (symmetric) and 65% (asymmetric) even at a higher scan rate of 100 mV/s. The asymmetric device exhibits an excellent energy density of 29.4 Wh/kg and a maximum power density of ∼133 kW/kg. It is also demonstrated that the materials can be used to fabricate a high specific capacitance all-solid-state flexible device with an ability to light up a 1.67 V LED when connected in series. This work opens the door for facile, robust, and scalable preparation strategy for low-cost, earth-abundant electrode materials for high-performance pseudocapacitor devices.

■ ASSOCIATED CONTENT

Supporting Information

The Supporting Information is available free of charge at https://pubs.acs.org/doi/10.1021/acsenergylett.9b02299.

Detailed experimental procedures, including microwave-assisted synthesis of the novel layered materials, structural analysis, BET, electrode fabrication, testing and device fabrication, and tables providing BET data, EIS data, and a comparison of energy and power densities (PDF)

■ AUTHOR INFORMATION

Corresponding Authors

*E-mail: kraju@csir.co.za (K.R.).

*E-mail: Kenneth.ozoemena@wits.ac.za (K.I.O.).

ORCID

Zheng Bo: 0000-0001-9308-7624

Kenneth I. Ozoemena: 0000-0001-7107-7003

Notes

The authors declare no competing financial interest.

■ ACKNOWLEDGMENTS

This work was supported by the South Africa's Council for Scientific and Industrial Research (CSIR), the National Research Foundation (NRF, Grant No. 113638), as well as the University of the Witwatersrand.

■ REFERENCES

(1) Lukatskaya, M. R.; Dunn, B.; Gogotsi, Y. Multidimensional Materials and Device Architectures for Future Hybrid Energy Storage. *Nat. Commun.* **2016**, *7*, 1−13.

(2) Chu, S.; Majumdar, A. Opportunities and Challenges for a Sustainable Energy Future. *Nature* **2012**, *488* (7411), 294−303.

(3) Dubal, D. P.; Ayyad, O.; Ruiz, V.; Gómez-Romero, P. Hybrid Energy Storage: The Merging of Battery and Supercapacitor Chemistries. *Chem. Soc. Rev.* **2015**, *44* (7), 1777−1790.

DOI: 10.1021/acsenergylett.9b02299
ACS Energy Lett. 2020, 5, 23−30

(4) Gogotsi, Y.; Simon, P. True Performance Metrics in Electrochemical Energy Storage. *Science* **2011**, *334* (6058), 917−918.
(5) Simon, P.; Gogotsi, Y. Materials for Electrochemical Capacitors. *Nat. Mater.* **2008**, *7* (11), 845−854.
(6) Xiong, T.; Tan, T. L.; Lu, L.; Lee, W. S. V.; Xue, J. Harmonizing Energy and Power Density toward 2.7 V Asymmetric Aqueous Supercapacitor. *Adv. Energy Mater.* **2018**, *8*, 1702630.
(7) Liu, B.-T.; Shi, X.-M.; Lang, X.-Y.; Gu, L.; Wen, Z.; Zhao, M.; Jiang, Q. Extraordinary Pseudocapacitive Energy Storage Triggered by Phase Transformation in Hierarchical Vanadium Oxides. *Nat. Commun.* **2018**, *9* (1), 1375.
(8) Feng, D.; Lei, T.; Lukatskaya, M. R.; Park, J.; Huang, Z.; Lee, M.; Shaw, L.; Chen, S.; Yakovenko, A. A.; Kulkarni, A.; et al. Robust and Conductive Two-Dimensional Metal-Organic Frameworks with Exceptionally High Volumetric and Areal Capacitance. *Nat. Energy* **2018**, *3* (1), 30−36.
(9) Sun, H.; Zhu, J.; Baumann, D.; Peng, L.; Xu, Y.; Shakir, I.; Huang, Y.; Duan, X. Hierarchical 3D Electrodes for Electrochemical Energy Storage. *Nat. Rev. Mater.* **2019**, *4*, 45.
(10) Yu, L.; Hu, L.; Anasori, B.; Liu, Y. T.; Zhu, Q.; Zhang, P.; Gogotsi, Y.; Xu, B. MXene-Bonded Activated Carbon as a Flexible Electrode for High-Performance Supercapacitors. *ACS Energy Lett.* **2018**, *3* (7), 1597−1603.
(11) Sarkar, D.; Das, D.; Das, S.; Kumar, A.; Patil, S.; Nanda, K. K.; Sarma, D. D.; Shukla, A. Expanding Interlayer Spacing in MoS2 for Realizing an Advanced Supercapacitor. *ACS Energy Lett.* **2019**, *4*, 1602−1609.
(12) Wu, C.; Lu, X.; Peng, L.; Xu, K.; Peng, X.; Huang, J.; Yu, G.; Xie, Y. Two-Dimensional Vanadyl Phosphate Ultrathin Nanosheets for High Energy Density and Flexible Pseudocapacitors. *Nat. Commun.* **2013**, *4*, 1−7.
(13) Li, Z.; Xu, Z.; Wang, H.; Ding, J.; Zahiri, B.; Holt, C. M. B.; Tan, X.; Mitlin, D. Colossal Pseudocapacitance in a High Functionality-High Surface Area Carbon Anode Doubles the Energy of an Asymmetric Supercapacitor. *Energy Environ. Sci.* **2014**, *7* (5), 1708−1718.
(14) He, W.; Wang, C.; Zhuge, F.; Deng, X.; Xu, X.; Zhai, T. Flexible and High Energy Density Asymmetrical Supercapacitors Based on Core/Shell Conducting Polymer Nanowires/Manganese Dioxide Nanoflakes. *Nano Energy* **2017**, *35* (March), 242−250.
(15) Brezesinski, T.; Wang, J.; Tolbert, S. H.; Dunn, B. Ordered Mesoporous α-MoO3with Iso-Oriented Nanocrystalline Walls for Thin-Film Pseudocapacitors. *Nat. Mater.* **2010**, *9* (2), 146−151.
(16) Zhu, Y.; Murali, S.; Stoller, M. D.; Ganesh, K. J.; Cai, W.; Ferreira, P. J.; Pirkle, A.; Wallace, R. M.; Cychosz, K. A.; Thommes, M.; et al. Carbon-Based Supercapacitors Produced by Activation of Graphene. *Science (Washington, DC, U. S.)* **2011**, *332* (6037), 1537−1541.
(17) Zhang, P.; Wang, F.; Yu, M.; Zhuang, X.; Feng, X. Two-Dimensional Materials for Miniaturized Energy Storage Devices: From Individual Devices to Smart Integrated Systems. *Chem. Soc. Rev.* **2018**, *47* (19), 7426−7451.
(18) Lukatskaya, M. R.; Kota, S.; Lin, Z.; Zhao, M. Q.; Shpigel, N.; Levi, M. D.; Halim, J.; Taberna, P. L.; Barsoum, M. W.; Simon, P.; et al. Ultra-High-Rate Pseudocapacitive Energy Storage in Two-Dimensional Transition Metal Carbides. *Nat. Energy* **2017**, *2*, 8.
(19) Okubo, M.; Sugahara, A.; Kajiyama, S.; Yamada, A. MXene as a Charge Storage Host. *Acc. Chem. Res.* **2018**, *51* (3), 591−599.
(20) Li, X.; Elshahawy, A. M.; Guan, C.; Wang, J. Metal Phosphides and Phosphates-Based Electrodes for Electrochemical Supercapacitors. *Small* **2017**, *13* (39), 1701530.
(21) Raju, K.; Ozoemena, K. I. Hierarchical One-Dimensional Ammonium Nickel Phosphate Microrods for High-Performance Pseudocapacitors. *Sci. Rep.* **2015**, *5*, 1−13.
(22) Sheberla, D.; Bachman, J. C.; Elias, J. S.; Sun, C. J.; Shao-Horn, Y.; Dincă, M. Conductive MOF Electrodes for Stable Supercapacitors with High Areal Capacitance. *Nat. Mater.* **2017**, *16* (2), 220−224.
(23) Wang, M.; Zhao, Y.; Zhang, X.; Qi, R.; Shi, S.; Li, Z.; Wang, Q.; Zhao, Y. Interface-Rich Core-Shell Ammonium Nickel Cobalt Phosphate for High-Performance Aqueous Hybrid Energy Storage Device without a Depressed Power Density. *Electrochim. Acta* **2018**, *272*, 184−191.
(24) Wang, S.; Pang, H.; Zhao, S.; Shao, W.; Zhang, N.; Zhang, J.; Chen, J.; Li, S. NH4CoPO4·H2O Microbundles Consisting of One-Dimensional Layered Microrods for High Performance Supercapacitors. *RSC Adv.* **2014**, *4* (1), 340−347.
(25) Coleman, J. N; Lotya, M.; O'Neill, A.; Bergin, S. D.; King, P. J.; Khan, U.; Young, K.; Gaucher, A.; De, S.; Smith, R. J.; et al. Two-Dimensional Nanosheets Produced by Liquid Exfoliation of Layered Materials. *Science (Washington, DC, U. S.)* **2011**, *331* (6017), 568−571.
(26) Wenwei, W.; Yanjin, F.; Xuehang, W.; Sen, L.; Shushu, L. Preparation via Solid-State Reaction at Room Temperature and Characterization of Layered Nanocrystalline NH4MnPO4·H2O. *J. Phys. Chem. Solids* **2009**, *70* (3−4), 584−587.
(27) Carling, S. G.; Day, P.; Vissen, D. Crystal and Magnetic Structures of Layer Transition Metal Phosphate Hydrates. *Inorg. Chem.* **1995**, *34* (15), 3917−3927.
(28) Koleva, V.; Stoyanova, R.; Zhecheva, E.; Nihtianova, D. Dittmarite Precursors for Structure and Morphology Directed Synthesis of Lithium Manganese Phospho-Olivine Nanostructures. *CrystEngComm* **2014**, *16* (32), 7515−7524.
(29) Teng, F.; Santhanagopalan, S.; Asthana, A.; Geng, X.; Mho, S., II; Shahbazian-Yassar, R.; Meng, D. D. Self-Assembly of LiFePO4 Nanodendrites in a Novel System of Ethylene Glycolwater. *J. Cryst. Growth* **2010**, *312* (23), 3493−3502.
(30) Ma, X.; Zhang, W.; Kong, L.; Luo, Y.; Kang, L. RSC Advances Electrochemical Performance in Alkaline and Neutral Electrolytes of a Manganese Phosphate Material Possessing a Broad Potential Window. *RSC Adv.* **2016**, *6*, 40077−40085.
(31) Pech, D.; Brunet, M.; Durou, H.; Huang, P.; Mochalin, V.; Gogotsi, Y.; Taberna, P.-L.; Simon, P. Ultrahigh-Power Micrometre-Sized Supercapacitors Based on Onion-like Carbon. *Nat. Nanotechnol.* **2010**, *5* (9), 651−654.
(32) Neher, G.; Salguero, T. T. δ-Polymorph of Manganese Phosphate. *Cryst. Growth Des.* **2017**, *17* (9), 4864−4872.
(33) Sharma, C. V. K.; Chusuei, C. C.; Clérac, R.; Möller, T.; Dunbar, K. R.; Clearfield, A. Magnetic Property Studies of Manganese-Phosphate Complexes. *Inorg. Chem.* **2003**, *42* (25), 8300−8308.
(34) Volkova, O. S.; Shvanskaya, L. V.; Ovchenkov, E. A.; Zvereva, E. A.; Volkov, A. S.; Chareev, D. A.; Molla, K.; Rahaman, B.; Saha-Dasgupta, T.; Vasiliev, A. N. Structure-Property Relationships in α-, B′-, and γ-Modifications of Mn 3 (PO 4) 2. *Inorg. Chem.* **2016**, *55* (20), 10692−10700.
(35) Jiang, Q.; Kurra, N.; Alhabeb, M.; Gogotsi, Y.; Alshareef, H. N. All Pseudocapacitive MXene-RuO $_2$ Asymmetric Supercapacitors. *Adv. Energy Mater.* **2018**, *8*, 1703043.
(36) Mwonga, P. V.; Barik, R.; Naidoo, S. R.; Quandt, A.; Ozoemena, K. I. *Phys. Chem. Chem. Phys.* **2018**, *20*, 28232−28240.
(37) Wang, Y.; Lai, W.; Wang, N.; Jiang, Z.; Wang, X.; Zou, P.; Lin, Z.; Fan, H. J.; Kang, F.; Wong, C. P.; et al. A Reduced Graphene Oxide/Mixed-Valence Manganese Oxide Composite Electrode for Tailorable and Surface Mountable Supercapacitors with High Capacitance and Super-Long Life. *Energy Environ. Sci.* **2017**, *10* (4), 941−949.
(38) Makgopa, K.; Raju, K.; Ejikeme, P. M.; Ozoemena, K. I. High-Performance Mn3O4/Onion-like Carbon (OLC) Nanohybrid Pseudocapacitor: Unravelling the Intrinsic Properties of OLC against Other Carbon Supports. *Carbon* **2017**, *117*, 20−32.
(39) Zhu, J.; Jiang, J.; Sun, Z.; Luo, J.; Fan, Z.; Huang, X.; Zhang, H.; Yu, T. 3D Carbon/Cobalt-Nickel Mixed-Oxide Hybrid Nanostructured Arrays for Asymmetric Supercapacitors. *Small* **2014**, *10* (14), 2937−2945.

DOI: 10.1021/acsenergylett.9b02299
ACS Energy Lett. 2020, 5, 23−30